PAPER

Au–ZnO hybrid nanoflowers, nanomultipods and nanopyramids: one-pot reaction synthesis and photocatalytic properties†

Yuanzhi Chen,* Deqian Zeng, Kun Zhang, Aolin Lu, Laisen Wang and Dong-Liang Peng*

The preparation of noble metal–semiconductor hybrid nanocrystals with controlled morphologies has received intensive interest in recent years. In this study, facile one-pot reactions have been developed for the synthesis of Au–ZnO hybrid nanocrystals with different interesting morphologies, including petal-like and urchin-like nanoflowers, nanomultipods and nanopyramids. In the synthesis strategy, oleylamine-containing solution serves as the reaction medium, and the *in situ* generated Au seeds play an important role in the subsequently induced growth of ZnO nanocrystals. With the aid of several surfactants, hybrid nanocrystals with different morphologies that have considerable influences on their optical and photocatalytic activities are readily achieved. Through high-resolution transmission electron microscopy measurements, an observed common orientation relationship between ZnO and Au is that ZnO nanocrystals prefer to grow with their polar {001} facets on the {111} facets of Au nanocrystals, and well-defined interfaces are evident. Surface plasmon resonance bands of Au with different positions are observed in the UV-vis spectra, and the UV and visible emissions of ZnO are found to be dramatically reduced. Finally, the as-prepared Au–ZnO nanocrystals exhibit excellent photocatalytic activity for the photodegradation of rhodamine B compared with pure ZnO nanocrystals. The Au–ZnO hybrid nanopyramids show the highest catalytic efficiency, which is correlated with the exposed crystal facets, crystallinity and the formation of hybrid nanostructures. The as-prepared Au–ZnO hybrid nanocrystals are expected to find diverse potential applications in the fields such as photocatalysis, solar energy conversion, sensing and biological detection.

Introduction

Combining different components at the nanoscale into a hybrid nanostructure has been an important research direction in the nanocrystal synthesis. Multicomponent hybrid nanostructures not only can harvest the multifunctionalities contributed from each component but also may obtain enhanced or even new functionalities due to synergetic effects between different components. For example, spin-polarized emission originating from hybridization of the magnetic and semiconducting materials has been observed.[1] Enhanced catalytic properties have been demonstrated in Ag@Ni core–shell nanoparticles[2] and Au–ZnO hybrid nanocrystals.[3] The recent progress in the synthesis and application of hybrid nanocrystals has been summarized in several reviews.[4–6]

Zinc oxide (ZnO) is an important semiconductor material that has a large direct band gap ($E_g = 3.37$ eV), a large excitation binding energy (60 meV), near-UV emission, transparent conductivity, and piezoelectricity.[7] Nanoscale ZnO materials have been widely applied in diverse technological fields among which photocatalysis is the one that has been receiving considerable attention. A copious amount of studies have been conducted on the synthesis and photocatalytic testing of ZnO nanocrystals for the degradation of organic pollutants in aqueous solution.[8–11] In the photocatalytic process, it is vital to achieve the photo-induced charge separation with the band gap excitation of the semiconductors. However, the quick recombination of the photo-excited electrons and holes in ZnO always leads to a reduced photocatalytic efficiency.

In order to restrain the recombination of photo-excited electrons and holes and enhance the photo-degradation efficiency of ZnO, one of the effective ways is to combine ZnO with metal nanoparticles to form a composite or hybrid structure. Noble metal nanoparticles such as Au, Ag and Pt have been used to combine with ZnO to achieve enhanced photocatalytic activities.[12–19] The involved mechanism is considered to be that

Department of Materials Science and Engineering, College, of Materials, Xiamen University, Xiamen, 361005, P.R. China. E-mail: yuanzhi@xmu.edu.cn; dlpeng@xmu.edu.cn; Fax: +86-592-2183515; Tel: +86-592-2188025

† Electronic supplementary information (ESI) available: EDS spectra, SEM images and TEM images of products synthesized under different conditions, and time-dependent UV-vis spectra recorded during the photocatalytic degradation of RhB by using different samples. See DOI: 10.1039/c3nr04558g

noble metals may act as a sink for photo-induced charge carriers and the presence of a metal semiconductor interface can promote effective charge separation and enhance interfacial charge-transfer. Choosing Au as the metal component for the formation of a hybrid nanostructure with ZnO not only can help obtain enhanced photocatalytic properties but also can bring in some other advantages, for example, improved sensing performances in CO[20] and ethanol[21] detection, and enhanced resonance Raman signals that can be used for ultrasensitive detection of DNA[22] and proteins.[23] Therefore the synthesis and application of Au–ZnO hybrid nanostructures have received intensive interest.

Although considerable efforts have been made on the synthesis of a series of Au–ZnO hybrid nanostructures,[12–15,20–33] many of the reported methods involve the uncontrolled deposition of Au nanoparticles on ZnO nanocrystals with different shapes and dimensions, and Au nanoparticles might be physically attached to ZnO. Recently several groups have achieved the synthesis of Au–ZnO hybrid nanopyramids in which Au nanoparticles can either locate at the tip or basal plane of ZnO nanopyramids.[15,31,32] On the whole, reports on the synthesis of Au–ZnO hybrid nanocrystals with other morphologies are not common. The rational synthesis of Au–ZnO hybrid nanocrystals with specific morphologies and well-defined interface which plays an important role in the charge distribution and consequently optical and photocatalytic properties still needs extra exploration.

In the present work, we report a simple one-pot non-aqueous synthetic route for the synthesis of Au–ZnO hybrid nanocrystals with multiple interesting morphologies, including petal-like and urchin-like nanoflowers, nanomultipods and nanopyramids. Unlike many reported syntheses in which metal nanoparticles are simply attached (no chemically bonded interface forms) onto ZnO surfaces, well-defined interfaces between ZnO and Au have been identified in this study. A preferred crystallographic relationship between ZnO and Au has also been observed. The influence of synthesis parameters on the hybrid morphology has been investigated. Finally we will show that the morphologies of the as-prepared hybrid nanocrystal affect their optical absorption spectra and photoluminescence (PL) spectra. Excellent photocatalytic activities for the degradation of rhodamine B have been observed. The synthesis strategy revealed in this study offers important clues for the preparation of metal–semiconductor hybrid nanocrystals with tunable morphologies.

Experimental section

Synthesis

Chemicals. Dibenzylether (BE) and oleylamine (OAm) were purchased from Acros. Other chemicals such as zinc stearate ($Zn(St)_2$), zinc acetate dehydrate ($Zn(OAc)_2 \cdot 2H_2O$), 1-hexadecanol (HDL), triphenyl phosphine (TPP), chloroauric acid tetrahydrate ($HAuCl_4 \cdot 4H_2O$), toluene, hexane, acetone, and ethanol were purchased from Sinopharm Chem. Reagent Co., Ltd. 1,2-Dodecandiol (DDL) was purchased from Aldrich. Rhodamine B was purchased from Xilong Chem. Co., Ltd. All reagents were used as received without further purification.

Synthesis of Au–ZnO nanoflowers. All of the preparations were carried out in an air-free atmosphere pre-purged by argon gas. In a typical synthesis of petal-like Au–ZnO nanoflowers (type-I), 0.02 mmol of $HAuCl_4 \cdot 4H_2O$, 0.74 mmol of DDL and 0.7 mmol of $Zn(OAc)_2 \cdot 2H_2O$ were added to a mixture of 2 mL of OAm and 5 mL of BE, and then heated to 120 °C for 15 min. Finally the solution was heated up to 260 °C for 1 h. After cooling to room temperature, the generated products were washed with hexane, ethanol and acetone several times, separated from solution by centrifugation, and then dried in a vacuum.

In a typical synthesis of urchin-like Au–ZnO nanoflowers (type-II), 0.02 mmol of $HAuCl_4 \cdot 4H_2O$, 0.1 mmol of TPP, and 0.24 mmol of $Zn(St)_2$ were added to 14 mL of OAm. Then the mixed solution was heated up to 280 °C and kept at this temperature for 1 h. The remaining steps are the same as those used for the preparation of petal-like Au–ZnO nanoflowers.

Synthesis of Au–ZnO nanomultipods. In a typical synthesis, 0.04 mmol of $HAuCl_4 \cdot 4H_2O$, 1.24 mmol of HDL, and 0.24 mmol of $Zn(St)_2$ were added to 14 mL of OAm, and then the mixed solution was heated to 120 °C for 15 min. Finally the solution was heated up to 280 °C and kept at this temperature for 1 h. The remaining steps are the same as those used for the preparation of Au–ZnO nanoflowers.

Synthesis of Au–ZnO nanopyramids. In a typical synthesis, 0.02 mmol of $HAuCl_4 \cdot 4H_2O$, 1.24 mmol of HDL and 0.24 mmol of $Zn(St)_2$ were added to a mixture of 2 mL of OAm and 5 mL of BE, and then heated to 120 °C for 15 min. Then the solution was heated up to 280 °C and kept at this temperature for 1 h. The remaining steps are the same as those used for the preparation of Au–ZnO nanoflowers.

Characterization

Powder X-ray diffraction (XRD) data were collected on a Panalytical X'pert PRO X-ray diffractometer using Cu K$_\alpha$ radiation. Transmission electron microscopy (TEM) was performed on TECNAI F-30 and JEM-2100 transmission electron microscopes. The TEM samples were prepared by sonicating the as-synthesized nanocrystals in toluene, and dropping a small volume onto a carbon-coated copper TEM grid followed by solvent evaporation. UV-visible spectra were recorded with a Cary-300 ultraviolet-visible spectrophotometer. Photoluminescence (PL) spectra were recorded in an FLS-920T fluorescence spectrophotometer using an excitation wavelength of 325 nm.

Photocatalytic testing

The photocatalytic activities of as-prepared Au–ZnO hybrid nanocrystals were tested by degrading an organic dye, rhodamine B (RhB) in aqueous solution. In the photocatalytic experiments, 10 mg of as-synthesized nanocrystals was added to a beaker containing 100 mL of RhB aqueous solution with a concentration of 1 mg L^{-1}, and the solution was stirred in the dark for 2 h to reach adsorption–desorption equilibrium between the catalyst and RhB. Then, the mixture was irradiated using a 175 W UV lamp. After the reaction mixture was irradiated for a given time, about 3 mL of the suspension was taken out and immediately centrifuged. The degradation of RhB was

monitored by measuring the absorbance of the solution using a Cary-300 UV-vis spectrophotometer.

Results and discussion

Synthesis and structural characterization

In this work, Au–ZnO hybrid nanoflowers were prepared with two types of morphologies, *i.e.* petal-like and urchin-like nanoflowers. Fig. 1a shows the low-magnification TEM image of the as-prepared petal-like Au–ZnO nanoflowers that actually have a core–shell structure consisting of an Au core and a ZnO shell. These nanoflowers have a typical size varying from 35 to 45 nm, and the size of the Au core is about 6–9 nm. The petal-like morphology can be clearly seen in the high-magnification TEM image shown in Fig. 1b. The high-resolution TEM (HRTEM) image (Fig. 1b, inset) taken from an individual Au–ZnO nanoflower shows lattice fringes belonging to the (111) plane of fcc Au in the center and to the (002) plane of wurtzite-type hexagonal ZnO at the edge portion, confirming the crystalline nature of Au and ZnO components. The near-parallel relationship between the (111) plane of Au and the (002) plane of ZnO also suggests that this ZnO petal grows with its basal facet on the basis of the Au (111) facet. The formed core–shell structure can be easily discerned from the high-angle annular dark-field (HAADF) image (Fig. 1c). Due to the stronger ability of Au than ZnO to scatter electrons, the Au cores appear much brighter in the HAADF image. Fig. 1d shows the compositional profile obtained by the energy-dispersive X-ray spectroscopy (EDS) line scanning performed in scanning TEM (STEM) mode from a single petal-like Au–ZnO nanoflower. It can be seen that

ZnO signals occur throughout the whole profile whereas Au signals only occur in the center, further confirming a core–shell structure. EDS spectra recorded from the center and edge clearly reveal signals belonging to Au and ZnO, respectively (Fig. S1†). The measured Au concentration (in at.%) in the whole hybrid nanocrystal is ∼8.4%. Control experiments were also conducted on the factors that influence the morphology of nanocrystals. The results show that the presence of DDL is very necessary for obtaining the petal-like morphology. If no DDL was added, detached bullet-like ZnO nanocrystals would be formed (Fig. S2†). Besides, the ratio of OAm and BE is also an important parameter. When only OAm was used, the morphology of Au–ZnO tended to be a round core–shell nanostructure (Fig. S3†). To maintain a petal-like morphology, the optimal volume ratio of OAm to BE should be from 1 : 1 to 2 : 5.

The urchin-like Au–ZnO nanoflowers were synthesized using $Zn(St)_2$ as a precursor in OAm without adding alkanol. In addition, TPP was added into the reaction to control the size of Au cores. Fig. 2a shows the TEM image of the urchin-like Au–ZnO nanoflowers prepared using the typical reaction with addition of 0.1 mmol of TPP. It can be seen that ZnO grows radially from the Au core in the form of short nanorods. The size of the Au core is about 20 nm while that of the whole particle is up to ∼100 nm. The measured Au concentration (in at.%) by EDS is ∼19.3%. When the quantities of TPP are increased to 0.5 mmol with other conditions fixed, the Au–ZnO hybrid nanocrystals still maintain a urchin-like morphology, however the Au core becomes much larger (80–100 nm) and the attached ZnO nanorods tend to be slim and their numbers increase. This result demonstrates that the Au core size of urchin-like Au–ZnO nanoflowers is tunable. The reason that the Au core size increases with the content of TPP is that TPP is a nucleation inhibitor that can form a stable complex with auric chloride. During the nucleation stage, the fast decomposition of the Au precursor is inhibited and the nuclei numbers are reduced. As a result, large Au cores are formed when the concentration of TPP increases in the reaction solution. Similar phenomena were observed in the Au seed-induced growth of Au@Ni nanoparticles wherein TPP served as a size controller for the Au core.[34]

The synthesis route for the Au–ZnO hybrid nanomultipods is similar to that of urchin-like nanoflowers except that surfactant TPP was replaced by HDL. Fig. 3a shows the low-magnification
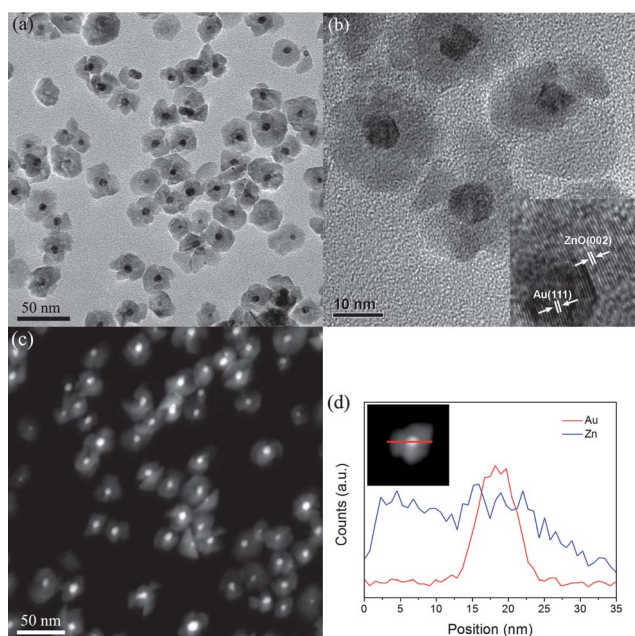

Fig. 1 TEM characterization of petal-like Au–ZnO nanoflowers. (a) Low-magnification TEM image. (b) High-magnification TEM image with an inset showing the lattice fringes belonging to Au and ZnO. (c) HAADF image. (d) STEM-EDS line-scan analysis of a single Au–ZnO nanoflower shown in the inset.
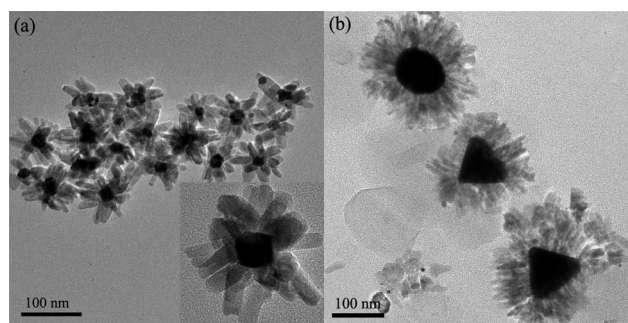

Fig. 2 TEM images of urchin-like Au–ZnO nanoflowers with small Au cores (a) and large Au cores (b). The inset in (a) is a magnified image of a single Au–ZnO nanoflower.
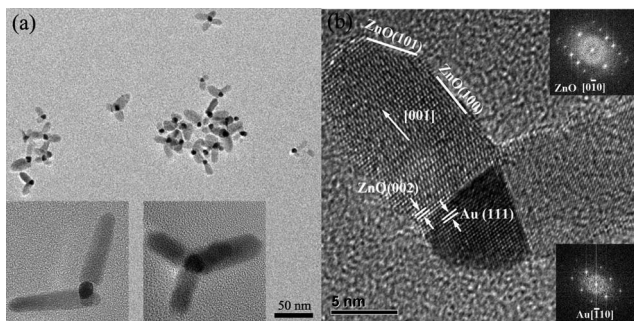
Fig. 3 (a) TEM image of Au–ZnO nanomultipods. The insets show the magnified images of di-pods and tri-pods. (b) HRTEM image of di-pods showing the crystalline planes of Au and ZnO. The insets are the FFT patterns of Au and ZnO.

TEM image of the as-prepared Au–ZnO hybrid nanomultipods that typically have a morphology consisting of an Au core connected by two or three ZnO nanorods, forming a hybrid structure of di-pods and tri-pods (see magnified images in the inset of Fig. 3a). The size of the Au core is about 7–9 nm while the length of the ZnO rods can vary from 13–30 nm. The measured Au concentration (in at.%) by EDS is ∼13.4%. The HRTEM image of individual Au–ZnO di-pods and their corresponding fast Fourier transform (FFT) patterns are shown in Fig. 3b. It reveals that the ZnO nanorod grows preferentially along its c-axis of the wurtzite structure. At the interface between Au and ZnO, the (002) plane of ZnO is found to be parallel to the (111) plane of Au, indicating that the basal plane of ZnO nanorods grows on the basis of Au (111) facets. The preferential orientation relationship can be described as $(001)_{ZnO}//(111)_{Au}$ and $[0\bar{1}0]_{ZnO}//[\bar{1}10]_{Au}$. HRTEM observation on other nanomultipods also reveals similar results (Fig. S4†). In addition, the tip of many ZnO nanorods is not ended by a flat (001) facet. Actually it forms a pyramid shape with the minimum exposure of the (001) facet. The reason is that the (001) facet is an unstable polar facet. If no effective capping agents are available, it will grow relatively fast and eventually becomes a pencil point in the growth process. It should be pointed out that the presence of HDL is important for obtaining a nanomultipod morphology. When no HDL is added, the nanomultipod morphology cannot be maintained and the morphology of ZnO will become a cuboid-like short rod with a flat end (Fig. S5†). Besides, the reaction temperature for the synthesis of Au–ZnO hybrid nanomultipods should be between 260 and 280 °C. A higher temperature and excess reaction time may lead to the coarsening of ZnO nanorods (Fig. S6†). These results reflect the sensitivity to the reaction parameters for the growth of Au–ZnO nanomultipods.

The preparation of Au–ZnO nanopyramids was reported very recently by several groups.[15,31,32] For example, Li et al. used a two step seed-mediated growth process to synthesize Au–ZnO nanopyramids.[15] Herring et al. obtained Au–ZnO hexagonal nanopyramids via a microwave irradiation method.[31] Herein we provide a non-aqueous one-step route for the synthesis of Au–ZnO nanopyramids. Interestingly, the preparation of Au–ZnO hybrid nanopyramids is on the basis of the method used for the preparation of Au–ZnO nanomultipods as

described previously with only a slight change in the synthesis conditions. Fig. 4a shows the low-magnification TEM image of the as-prepared Au–ZnO hybrid nanopyramids and the magnified images of di-pyramids and tri-pyramids (inset of Fig. 4a). It can be seen that one Au core typically can combine with two to four ZnO nanopyramids, forming a multipyramid structure. The Au core size is about 5–9 nm and the lengths of the side edge of ZnO nanopyramids are in the range of 25–34 nm. The pyramid morphology with the hexagonal basal plane of ZnO can be clearly seen in the SEM image (Fig. S7†). The measured Au concentration (in at.%) by EDS is ∼6.7%. The HRTEM image (Fig. 4b) of an individual hybrid nanocrystal presents the lattice fringes belonging to the well-defined (111) plane of fcc Au and the (002) plane of wurtzite-type ZnO, respectively. The (002) plane of ZnO is also found to be parallel to the (111) plane of Au, indicating that the growth of the ZnO pyramid takes place on the (111) facet of the Au seed. The employment of a mixed solvent is found to be helpful for the formation of the nanopyramid morphology. When sole OAm was used as the solvent, the morphology of ZnO would change from nanopyramid to nanomultipod (see Fig. S8†). The reason is unclear yet; probably a relatively high concentration of OAm may promote the growth of ZnO along its c-axis to achieve a rod like morphology.

The XRD patterns of Au–ZnO hybrid nanocrystals prepared using the typical syntheses with four different morphologies are shown in Fig. 5. All samples exhibit diffraction peaks that can be assigned to the wurtzite-type ZnO and fcc Au, and no other crystalline impurities can be observed in the diffraction patterns. The differences in the morphology and size of Au–ZnO hybrid nanocrystals are reflected from the XRD patterns. For the petal-like nanoflowers, the diffraction peaks of Au are broad and weak, which is mainly due to the small dimensions of Au cores. In contrast, the Au diffraction peaks of the urchin-like nanoflowers (shown in Fig. 2a) become much stronger and narrower due to the inclusion of Au cores with a rather large size. The nanomultipod sample also exhibits broad and relatively weak Au diffraction peaks compared to the petal-like nanoflowers; however the intensity is increased since the ZnO nanorods are short and do not fully cover the Au cores. In addition, the (002) diffraction peak of ZnO is stronger compared with other three samples, which indicates a preferred growth along the c-axis of ZnO nanorods. The highly crystalline
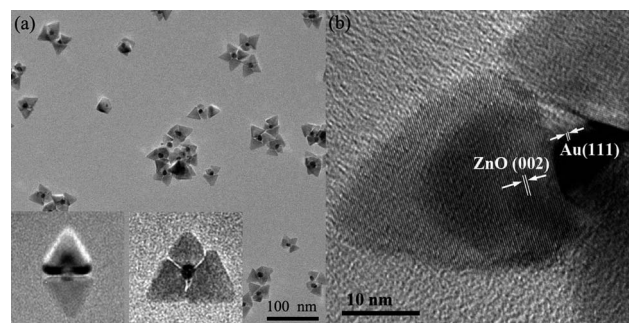

Fig. 4 (a) TEM image of Au–ZnO nanopyramids. The insets show the magnified images of di-pyramids and tri-pyramids. (b) HRTEM image of an Au–ZnO nanopyramid showing the lattice fringes belonging to Au and ZnO.
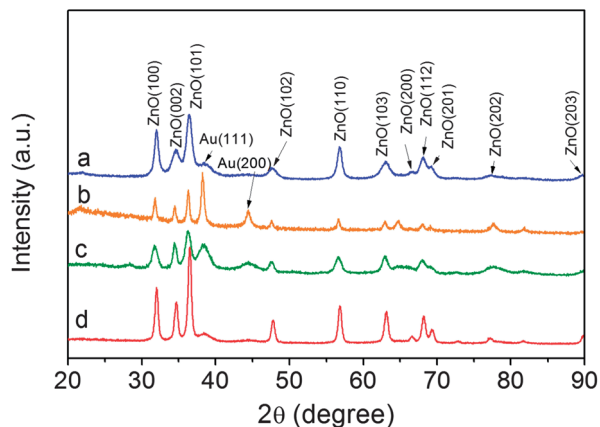
Fig. 5 XRD patterns of Au–ZnO petal-like nanoflowers (a), urchin-like nanoflowers (b), nanomultipods (c), and nanopyramids (d).

structure of ZnO nanopyramids can be revealed from their well-defined geometry shown in the TEM image and strong and narrow diffraction peaks. The stronger (101) diffraction peak also reflects the side facets of nanopyramids. The observed structural differences of ZnO nanocrystals affect their photo-catalytic properties that will be discussed later.

From the above experimental results, the overall scheme for the preparation of Au–ZnO hybrid nanocrystals with four different morphologies is summarized in Scheme 1. It is believed that Au can act as a nucleation site for the growth of heterogeneous shells.[4,35,36] In OAm-containing solution, OAm can serve both as a solvent and a reducing agent. Au(III) species can be reduced by OAm to Au(0) atoms which will undergo the nucleation and growth stage, and eventually develop into Au nanocrystal seeds. As soon as Au nanocrystals form, they can further catalyze the nucleation of ZnO, which has a great influence on the final morphologies of ZnO. In the absence of Au nanocrystals, none of the morphologies of ZnO described previously can be formed. As a fcc noble metal, Au nanocrystals usually are enclosed by low-index {111} and {100} facets that have low surface energies. The atoms on {111} facets of Au have

a hexagonal arrangement while those on {100} facets have a square close-packed arrangement. Since the basal {001} facets of hexagonal ZnO have the same hexagonal arrangement as that of {111} facets of Au, ZnO will tend to preferentially grow on the {111} facets of Au to reduce the large lattice mismatch. This could be a possible reason for explaining the observed crystal-lographic relationship between ZnO and Au. This growth manner of ZnO with its polar plane combining with Au {111} facets can lead to the lower interface energy and form a stable interface, which is conducive for the ZnO development into the specific morphology.

On the other hand, the employed solvent and surfactants also play an important role in determining the final morphologies of ZnO. During the synthesis of petal-like Au–ZnO nanoflowers, solvent BE which contains aromatic rings can act as electron donors to replenish the electronic deficiency, which is helpful for the nucleation on multiple facets. The precursor $Zn(OAc)_2 \cdot 2H_2O$ is also easier to decompose than $Zn(St)_2$. In the mean time, DDL which has a certain reducing ability due to its two hydroxyl groups can help to create multiple nucleation sites for ZnO on Au surfaces. Consequently, ZnO can freely grow around the Au core and eventually form a petal-like core–shell structure. In the synthesis of Au–ZnO hybrid nanopyramids, DDL is replaced by HDL that has only one hydroxyl group, which may reduce the nucleation sites for ZnO. In addition, $Zn(St)_2$ that has a higher decomposition temperature is used as the ZnO precursor. Therefore it can ensure a relatively slow growth environment for the formation of ZnO nanocrystals with a pyramid shape. Similar to the case of nanopyramids, the nucleation sites for the growth of nanomultipods are also limited due to the use of HDL. However, the high concentration of OAm (no BE added) may be favourable for maintaining the rod structure. Finally, in the synthesis of urchin-like Au–ZnO nanoflowers, TPP plays an important role. As discussed previously, TPP can form a stable complex with auric chloride, thus reducing the nucleation of Au and resulting in large Au cores that can provide more growth sites for ZnO to form an urchin-like morphology.

Optical properties

Fig. 6 presents the UV-vis spectra of the as-prepared Au–ZnO hybrid nanocrystals with four different morphologies. Two major absorption bands are observed for all these samples. The band at about 355–365 nm corresponds to the band gap absorption of ZnO while the one varying around 510–565 is attributed to surface plasmon resonance (SPR) absorption of Au. Compared to the nanopyramid sample which has a ZnO absorption band at 365 nm, the samples of petal-like nano-flowers, urchin-like nanoflowers and nanomultipods show a slight blue shift on the ZnO absorption band. This may be due to the smaller ZnO dimensions of the later three samples. The SPR bands of Au for the petal-like nanoflowers, urchin-like nanoflowers, nanomultipods and nanopyramids are at 545, 563, 538 and 513 nm, respectively. The observed different positions of the SPR band can be ascribed to two major reasons, *i.e.* the size of Au cores and the covering manner of ZnO. Generally, the SPR band of Au nanoparticles red shifts with increasing size.
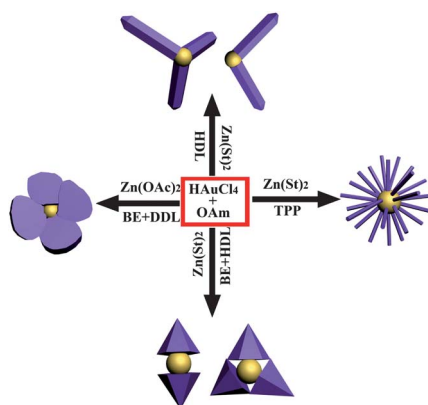
Scheme 1 Illustration of the synthesis routes for Au–ZnO hybrid nanocrystals with different morphologies.
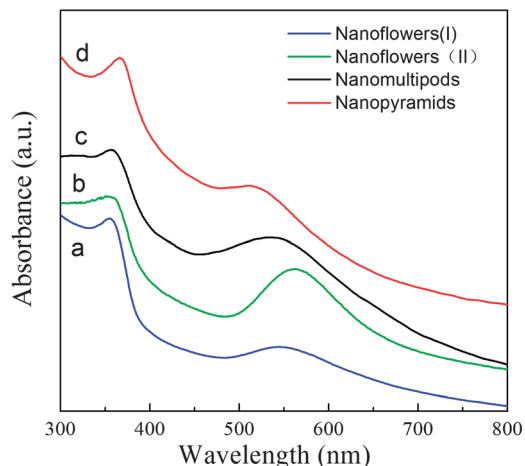
Fig. 6 UV-vis spectra of Au–ZnO petal-like nanoflowers (type I) (a), urchin-like nanoflowers (type II) (b), nanomultipods (c), and nano-pyramids (d).

Since the urchin-like nanoflowers have the largest Au cores, the red shift of the SPR band of Au is very distinct. Furthermore, an oxide shell (*e.g.* ZnO, TiO$_2$ and SnO$_2$) that has a high dielectric constant can cause a red shift in the SPR absorption of the Au core.[37,38] Compared to the nanomultipod and nanopyramid samples, the flower-like Au–ZnO sample has a more dense covering of the ZnO shell, which certainly is helpful for the red-shift of the SPR band of Au. As a result, this red-shift effect is also obvious in the flower-like Au–ZnO sample.

Fig. 7 shows the representative PL spectra of the Au–ZnO hybrid nanocrystals with the same examined amount obtained with the excitation wavelength of 325 nm at room temperature. For the purpose of comparison, the spectrum is also included for ZnO nanocrystals (Fig. S9†) that were synthesized using the same method for preparing petal-like Au–ZnO nanoflowers except that no Au precursor was added. The PL spectrum of the ZnO nanocrystals (curve a) possesses a feature that consists of
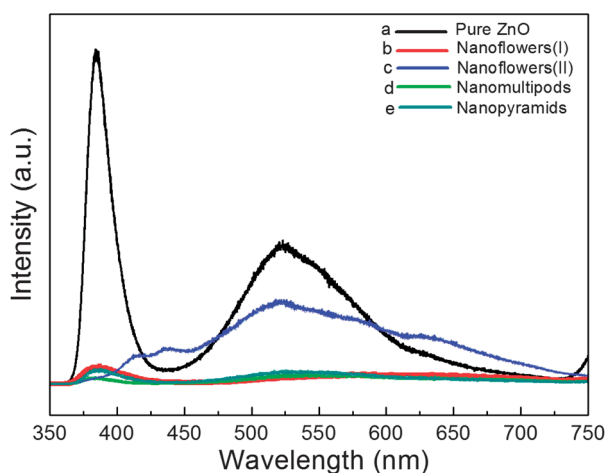
two emission bands in the UV-visible range, *i.e.* one is the UV near-band-edge (NBE) emission centered at ~385 nm and the other is a broad green region centered at ~525 nm. The UV emission can be attributed to the recombination of free exci-tons, and the green emission may arise from the recombination of photo-generated holes with the electrons in singly occupied oxygen vacancies.[39,40] Compared with the ZnO nanocrystals, the UV emission of Au–ZnO hybrid nanocrystals is dramatically reduced, indicating the decreased electron–hole recombina-tion. The visible emissions of Au–ZnO petal-like nanoflowers, nanomultipods and nanopyramids are also greatly reduced compared with the strong peak centered at 525 nm in the PL spectrum of ZnO. A possible reason is that the surface oxygen vacancies are mostly quenched due to the formation of the metal–ZnO interface. The urchin-like Au–ZnO nanoflowers (curve c) show a distinct curve that contains four weak emis-sions centers at 385 (very weak intensity), 417, 434 and 630 nm, respectively, besides the dominant one at 524 nm. The weak emissions at 417 and 434 nm may originate from electronic transitions from different energy levels of intrinsic defects, however further clarification is needed. The relatively strong and broad green emission of urchin-like Au–ZnO nanoflowers compared to other hybrid nanocrystals implies the increase of structural defects, such as oxygen vacancies and zinc intersti-tials. It also indicates the decrease in crystallinity of ZnO, which will consequently affect the photocatalytic activities.

Evaluation of photocatalytic efficiency

Photocatalytic activities of the as-synthesized Au–ZnO hybrid nanocrystals were evaluated by decomposing RhB in aqueous solutions under UV irradiation. The absorption profiles of RhB during the photocatalytic process are presented in Fig. 8. For the convenience of comparison, the irradiation time is kept at 30 min. The sample without adding any catalysts shows a strong absorp-tion peak centered at about 550 nm (Fig. 8, curve a). For pure ZnO nanocrystals (Fig. S9†), the concentration of RhB is reduced by about 29%. However, distinctly enhanced photocatalytic efficien-cies are observed with the addition of Au–ZnO hybrid nano-crystals, which is evidenced by the rapid decrease of the main absorption peak intensity. Especially, it can be observed that RhB is almost completely degraded by the Au–ZnO nanopyramids within 30 min (Fig. 8, curve f). By comparing the photocatalytic activities of the four different Au–ZnO hybrid nanocrystals, from the highest to the lowest in rank, they are: Au–ZnO nanopyramids, nanomultipods, urchin-like nanoflowers and petal-like nano-flowers. More details about the time-dependent photocatalytic degradation profiles are available in Fig. S10.†

The observed photocatalytic activity among different cata-lysts is at first related to the shape and exposed facets of ZnO. The ZnO crystal is a polar crystal which can be regarded as alternating planes comprising tetrahedrally coordinated O^{2-} and Zn^{2+} ions, stacked alternatively along the *c*-axis. Generally, the non-polar facets such as {100} and {110} are more stable than the polar {001} facets. Therefore the nanopyramids that have a relatively large area of exposed polar {001} facets are likely to have the highest photocatalytic activities, whereas the

Fig. 7 Room temperature PL spectra of pure ZnO nanocrystals (a), petal-like Au–ZnO nanoflowers (type I) (b), urchin-like Au–ZnO nanoflowers (type II) (c), Au–ZnO nanomultipods (d), and Au–ZnO nanopyramids (e).
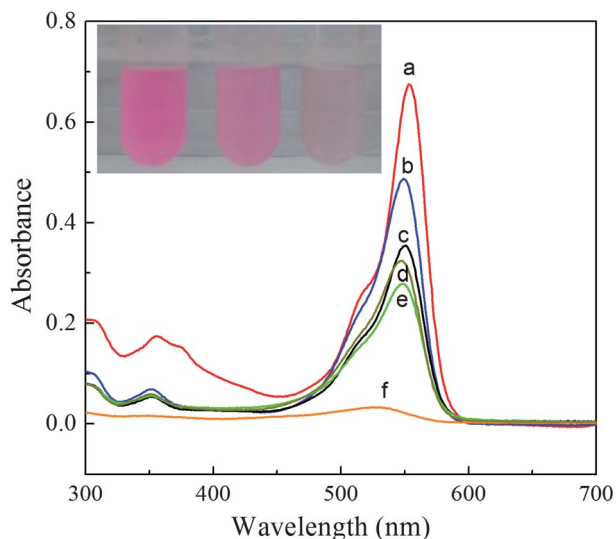
Fig. 8 UV-vis spectra recorded during the photocatalytic degradation of RhB by using different catalysts. (a) Without adding any catalysts. (b) ZnO nanocrystals. (c) Petal-like Au–ZnO nanoflowers. (d) Urchin-like Au–ZnO nanoflowers. (e) Au–ZnO nanomultipods. (f) Au–ZnO nanopyramids. The reaction time for curves (b)–(f) is all 30 min for the convenience of comparison. The inset demonstrates the color change after adding Au–ZnO nanomultipods for 0, 30 and 60 min, respectively (from left to right).

Au–ZnO nanomultipods and urchin-like nanoflowers that basically have a rod structure with mainly exposed {100} and {110} facets exhibit less superior photocatalytic activities. This facet-sensitive photocatalytic property has been demonstrated in ZnO nanodisks that have a high {001} facet population and the best photocatalytic activity.[41] In addition, since the nanopyramids have the best crystallinity (see the XRD pattern in Fig. 5) compared with other samples, the well-crystallized structure with less number of defects can help to improve the charge transfer, therefore improving the photocatalytic efficiency. Finally, the well defined interface between Au and ZnO after the formation of the hybrid structure can also play an important role in the enhancement of photocatalytic activities. When electrons are excited from the valence band to the conduction band of ZnO, they leave behind the same amount of holes in the valence band. Since the newly formed Fermi energy level of the Au–ZnO heterostructures is lower than the energy level of the bottom of the conduction band of ZnO, the photoexcited electrons will transfer from ZnO to Au driven by the energy difference. A calculation on the density of states (DOS) on the Au–ZnO composites indicates the existence of abundant empty Au states within the ZnO band gap.[32] In such a situation, Au acts as an electron accepting species at the Au–ZnO interface and can suppress the photo-excited electron–hole recombination, promote the transport of interface charges, and thus lead to enhanced photocatalytic activities. The trapping of the photo-excited charge carriers can also be revealed from the PL spectra in which the UV emission of ZnO is greatly damped. Hence, based on the observed experimental facts, the photocatalytic properties of Au–ZnO hybrid nanocrystals are correlated with multiple factors such as morphology, exposed facets and

crystallinity of ZnO and the formation of a hybrid structure, all of which should be taken into account in the rational design of Au–ZnO hybrid nanocrystal catalysts.

Conclusions

In summary, Au–ZnO hybrid nanocrystals with four interesting morphologies, *i.e.* petal-like and urchin-like nanoflowers, nanomultipods and nanopyramids have been prepared *via* a simple one-pot non-aqueous synthesis strategy. It is notable that a small difference in experimental conditions can make a large difference in the morphology and properties of Au–ZnO hybrid nanocrystals. An observed fact for the orientation relationship between ZnO and Au is that ZnO nanocrystals prefer to grow with their polar {001} facets on the {111} facets of Au nanocrystals. Surfactants play an important role in morphological control of the as-prepared hybrid nanocrystals. DDL is found to be necessary for the creation of multiple nucleation sites for obtaining a core–shell structured petal-like morphology, while TPP is effective for adjusting the size of Au cores. The UV-vis spectra show different positions of SPR bands of Au, which is related to the size of Au nanocrystals and the covering manner of ZnO. The UV emission of Au–ZnO hybrid nanocrystals is found to be dramatically reduced, indicating the suppression of the electron–hole recombination. Finally, all Au–ZnO hybrid nanocrystals exhibit excellent photocatalytic properties in the photodegradation of RhB in aqueous solutions. Especially Au–ZnO nanopyramids show the highest photocatalytic activity, which may be attributed to the larger exposed polar {001} facets, better crystallinity as well as the formation of a hybrid structure with a well defined interface. It is expected that the as-prepared Au–ZnO hybrid nanocrystals may have various technological applications such as in photocatalysis, solar energy conversion, sensing and biological detection.

Acknowledgements

References

1 B. T. Jonker, Y. D. Park, B. R. Bennett, H. D. Cheong, G. Kioseoglou and A. Petrou, *Phys. Rev. B: Condens. Matter Mater. Phys.*, 2000, **62**, 8180–8183.
2 H. Guo, Y. Chen, X. Chen, R. Wen, G.-H. Yue and D.-L. Peng, *Nanotechnology*, 2011, **22**, 195604.
3 M. Ahmad, Y. Shi, A. Nisar, H. Sun, W. Shen, M. Wei and J. Zhu, *J. Mater. Chem.*, 2011, **21**, 7723–7729.
4 H. Zeng and S. Sun, *Adv. Funct. Mater.*, 2008, **18**, 391–400.
5 R. Costi, A. E. Saunders and U. Banin, *Angew. Chem., Int. Ed.*, 2010, **49**, 4878–4897.

6 M. B. Cortie and A. M. McDonagh, *Chem. Rev.*, 2011, **111**, 3713–3735.

7 X. Wang, Y. Ding, C. J. Summers and Z. L. Wang, *J. Phys. Chem. B*, 2004, **108**, 8773–8777.

8 S. Chakrabarti and B. K. Dutta, *J. Hazard. Mater. B*, 2004, **112**, 269–278.

9 M. A. Behnajady, N. Modirshahla and R. Hamzavi, *J. Hazard. Mater.*, 2006, **133**, 226–232.

10 C. Hariharan, *Appl. Catal., A*, 2006, **304**, 55–61.

11 H. Wang, C. Xie, W. Zhang, S. Cai, Z. Yang and Y. Gui, *J. Hazard. Mater.*, 2007, **141**, 645–652.

12 J.-J. Wu and C.-H. Tseng, *Appl. Catal., B*, 2006, **66**, 51–57.

13 P. Pawinrat, O. Mekasuwandumrong and J. Panpranot, *Catal. Commun.*, 2009, **10**, 1380–1385.

14 Q. Wang, B. Y. Geng and S. Z. Wang, *Environ. Sci. Technol.*, 2009, **43**, 8968–8973.

15 P. Li, Z. Wei, T. Wu, Q. Peng and Y. Li, *J. Am. Chem. Soc.*, 2011, **133**, 5660–5663.

16 Y. Zheng, L. Zheng, Y. Zhan, X. Lin, Q. Zheng and K. Wei, *Inorg. Chem.*, 2007, **46**, 6980–6986.

17 H. R. Liu, G. X. Shao, J. F. Zhao, Z. X. Zhang, Y. Zhang, J. Liang, X. G. Liu, H. S. Jia and B. S. Xu, *J. Phys. Chem. C*, 2012, **116**, 16182–16190.

18 M. E. Aguirre, H. B. Rodríguez, E. S. Román, A. Feldhoff and M. A. Grela, *J. Phys. Chem. C*, 2011, **115**, 24967–24974.

19 J. Yuan, E. S. G. Choo, X. Tang, Y. Sheng, J. Ding and J. Xue, *Nanotechnology*, 2010, **21**, 185606.

20 S. J. Chang, T. J. Hsueh, I. C. Chen and B. R. Huang, *Nanotechnology*, 2008, **19**, 175502.

21 X. H. Liu, J. Zhang, X. Z. Guo, S. H. Wu and S. R. Wang, *Nanoscale*, 2010, **2**, 1178–1184.

22 Y. Liu, M. Zhong, G. Shan, Y. Li, B. Huang and G. Yang, *J. Phys. Chem. B*, 2008, **112**, 6484–6489.

23 G. Shan, S. Wang, X. Fei, Y. Liu and G. Yang, *J. Phys. Chem. B*, 2009, **113**, 1468–1472.

24 J. Geng, G.-H. Song, X.-D. Jia, F.-F. Cheng and J.-J. Zhu, *J. Phys. Chem. C*, 2012, **116**, 4517–4525.

25 C. K. N. Peh, L. Ke and G. W. Ho, *Mater. Lett.*, 2010, **64**, 1372–1375.

26 K. K. Haldar, T. Sen and A. Patra, *J. Phys. Chem. C*, 2008, **112**, 11650–11656.

27 B. Chen, H. Zhang, N. Du, D. Li, X. Ma and D. Yang, *Mater. Res. Bull.*, 2009, **44**, 889–892.

28 M.-K. Lee, T. G. Kim, W. Kim and Y.-M. Sung, *J. Phys. Chem. C*, 2008, **112**, 10079–10082.

29 X. Wang, X. G. Kong, Y. Yu and H. Zhang, *J. Phys. Chem. C*, 2007, **111**, 3836–3841.

30 L. Wang, Y. Sun, J. Wang, J. Wang, A. Yu, H. Zhang and D. Song, *J. Colloid Interface Sci.*, 2010, **351**, 392–397.

31 N. P. Herring, K. AbouZeid, M. B. Mohamed, J. Pinsk and M. S. El-Shall, *Langmuir*, 2011, **27**, 15146–15154.

32 K. X. Yao, X. Liu, L. Zhao, H. C. Zeng and Y. Han, *Nanoscale*, 2011, **3**, 4195–4200.

33 M. N. Tahir, F. Natalio, M. A. Cambaz, M. Panthöfer, R. Branscheid, U. Kolbb and W. Tremel, *Nanoscale*, 2013, **5**, 9944–9949.

34 H. She, Y. Chen, X. Chen, K. Zhang, Z. Wang and D.-L. Peng, *J. Mater. Chem.*, 2012, **22**, 2757–2765.

35 D. Wang and Y. Li, *J. Am. Chem. Soc.*, 2010, **132**, 6280–6281.

36 W. Shi, H. Zeng, Y. Sahoo, T. Y. Ohulchanskyy, Y. Ding, Z. L. Wang, M. Swihart and P. N. Prasad, *Nano Lett.*, 2006, **6**, 875–881.

37 X.-F. Wu, H.-Y. Song, J.-M. Yoon, Y.-T. Yu and Y.-F. Chen, *Langmuir*, 2009, **25**, 6438–6447.

38 G. Oldfield, T. Ung and P. Mulvaney, *Adv. Mater.*, 2000, **12**, 1519–1522.

39 B. Marí, F. J. Manjón, M. Mollar, J. Cembrero and R. Gómez, *Appl. Surf. Sci.*, 2006, **252**, 2826–2831.

40 K. Vanheusden, W. L. Warren, C. H. Seager, D. K. Tallant, J. A. Voigt and B. E. Gnade, *J. Appl. Phys.*, 1996, **79**, 7983–7990.

41 J. H. Zeng, B. B. Jin and Y. F. Wang, *Chem. Phys. Lett.*, 2009, **472**, 90–95.